Additive Manufacturing 29 (2019) 100808

Contents lists available at ScienceDirect

Additive Manufacturing

journal homepage: www.elsevier.com/locate/addma

Full length article

Residual stresses and distortion in the patterned printing of titanium and nickel alloys

Qianru Wu[a,b], Tuhin Mukherjee[b], Changmeng Liu[a,*], Jiping Lu[a], Tarasankar DebRoy[b,*]

[a] School of Mechanical Engineering, Beijing Institute of Technology, Beijing 100081, China
[b] Department of Materials Science and Engineering, The Pennsylvania State University, University Park, PA 16802, USA

ARTICLE INFO

Keywords:
Wire arc additive manufacturing
Delamination
Warping
Strain parameter
Scanning strategy

ABSTRACT

Since the deposition patterns affect the stresses and distortions, we examined their effects on multi-layer wire arc additive manufacturing (WAAM) of Ti-6Al-4V and Inconel 718 components experimentally and theoretically. We measured residual stresses by hole drilling method in three identical components printed using different deposition patterns. In order to understand the origin and the temporal evolution of residual stresses and distortion, we used a well-tested thermo-mechanical model after validating the computed results with experimental data for different deposition patterns. Distortions were also examined based on non-dimensional analysis.

We show that printing with short track lengths can minimize residual stresses and distortion among the three patterns investigated for both alloys. Both Ti-6Al-4V and Inconel 718 had similar fusion zone shape and size and were equally susceptible to deformation and warping, although Ti-6Al-4V was relatively less vulnerable to delamination due to its higher yield strength. A dimensionless strain parameter accurately predicted the effects of WAAM parameters on distortion and this approach is especially useful when the detailed thermo-mechanical calculations cannot be undertaken.

1. Introduction

Wire arc additive manufacturing (WAAM) is one of the common additive manufacturing (AM) processes for alloys and is widely used for rapid production because of the high melting and deposition rates [1]. However, these desirable attributes also make the WAAM components susceptible to residual stresses and distortion that often result in delamination and warping of the parts [2–4]. Residual stresses and distortion primarily depend on transient temperature field, deposition patterns and alloy used. Therefore, controlling delamination and warping requires a better understanding of the evolution of residual stresses and distortion depending on the transient temperature field for different deposition patterns and alloys.

Several attempts have been made to evaluate the roles of deposition patterns on residual stresses and distortion in WAAM. For example, Somashekara et al. [5] proved that the residual stresses and distortion in a single layer steel component can be controlled by adjusting the deposition sequence. The components deposited by linear raster pattern exhibited lower residual stresses than that in the part printed with spiral patterns [5]. The distortion of a panel structure could be minimized by choosing a proper building sequence [6]. For a thin wall structure, the component deposited using bi-directional scanning was found to exhibit lower residual stresses and the maximum plastic strain when compared to that printed using unidirectional scanning [7]. It was reported that for mild steel components, deposition sequences do not have any effect on reducing the deflection but can alter the residual stress distribution [8]. The effect of deposition patterns on stresses and deformation was also studied for steel components printed using WAAM [9]. However, these aforementioned researches are unable to conclude whether the observed effects of deposition patterns on residual stresses and distortion are consistent for various AM alloys. The literature investigating the role of alloys on residual stresses and distortion of WAAM components is scarce. Only Oyama et al. [10] showed that the residual stresses in thin walls of two aluminum alloys can be different because of the differences in their thermo-physical and mechanical properties. Therefore, what is needed and currently not available is the detailed understanding of the simultaneous effects of the deposition patterns and the nature of the alloys on the evolution of stresses and distortion during multi-layer WAAM.

It was reported in the literature that residual stresses and distortion evolve based on the spatial and temporal variations of the temperature field [11]. Since in-situ measurement of stresses during printing is difficult, experimentally it is often impossible to investigate the evolution of stress fields. A recourse is to use a well-tested thermo-

* Corresponding authors.
E-mail addresses: liuchangmeng@bit.edu.cn (C. Liu), debroy@psu.edu (T. DebRoy).

https://doi.org/10.1016/j.addma.2019.100808
Received 13 June 2019; Received in revised form 19 July 2019; Accepted 25 July 2019
Available online 01 August 2019
2214-8604/ Published by Elsevier B.V.

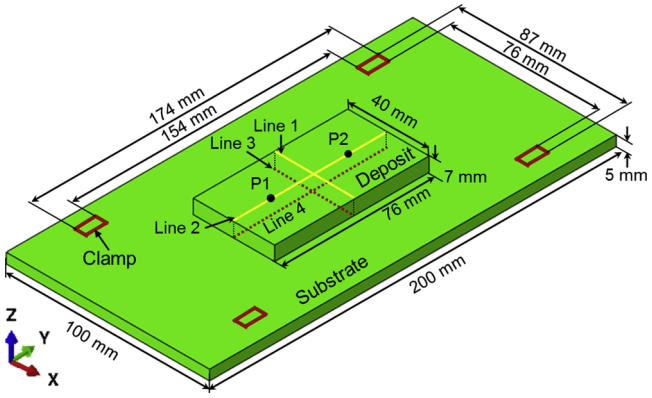

Fig. 1. Dimensions of the deposit and substrate. The clamps position and the four lines along which calculated data are extracted are shown. Line 1 and 2 are on the top surface of the deposit. Line 3 and 4 are at the substrate-deposit interface where the data for warping and delamination are examined. The measuring points of von Mises stress (P1 and P2) using the hole drilling method are also shown.

mechanical model of the WAAM process. This model first calculates the 3D, transient temperature field based on which residual stresses and distortions are predicted for different alloys and deposition patterns. Convective heat flow aided by Marangoni effect owing to the surface tension gradient inside the liquid pool is often the main mechanism of heat transfer inside the molten pool and thus affects the temperature fields and fusion zone shape and size. For example, Manvatkar et al. [12] reported that numerical calculations without considering the effect of convective flow severely overestimated the peak temperature inside the molten pool. Therefore, it is important to examine the role of fluid flow on transient temperature fields to obtain accurate results for the thermo-mechanical calculations.

Here, we conduct a combined theoretical and experimental research to investigate the evolution of stresses and distortion based on transient temperature fields during multi-layer, multi-hatch WAAM components of two alloys, Ti-6Al-4V and Inconel 718, with three different deposition patterns. We (a) print identical components using three different deposition patterns and measure residual stresses using hole drilling method, (b) use a thermo-mechanical model to calculate the 3D distribution of residual stresses and distortion and compare the results with the experiments, (c) examine the effects of molten metal convection on the calculated results, (d) compare the susceptibilities to delamination and warping of Ti-6Al-4V and Inconel 718 (IN 718) and (e) introduce back-of-the-envelope calculations using dimensionless strain parameter to predict the effects of WAAM parameters on distortion which is useful when the detailed thermo-mechanical calculations cannot be undertaken.

2. Fabrication of the components and residual stresses measurement

Rectangular deposits were printed using a WAAM equipment that

Table 1
Process parameters.

Average current (A)	Average voltage (V)	Arc efficiency	Welding speed (mm/s)	Heat input (J/mm)*	Wire feeding speed (mm/s)	Wire diameter (mm)	Layer thickness (mm)	Hatch distance (mm)
53.6	13	0.7	2	244	16.7	1.2	1.4	4

* Heat input = (Arc voltage * arc current * arc efficiency) / welding speed.

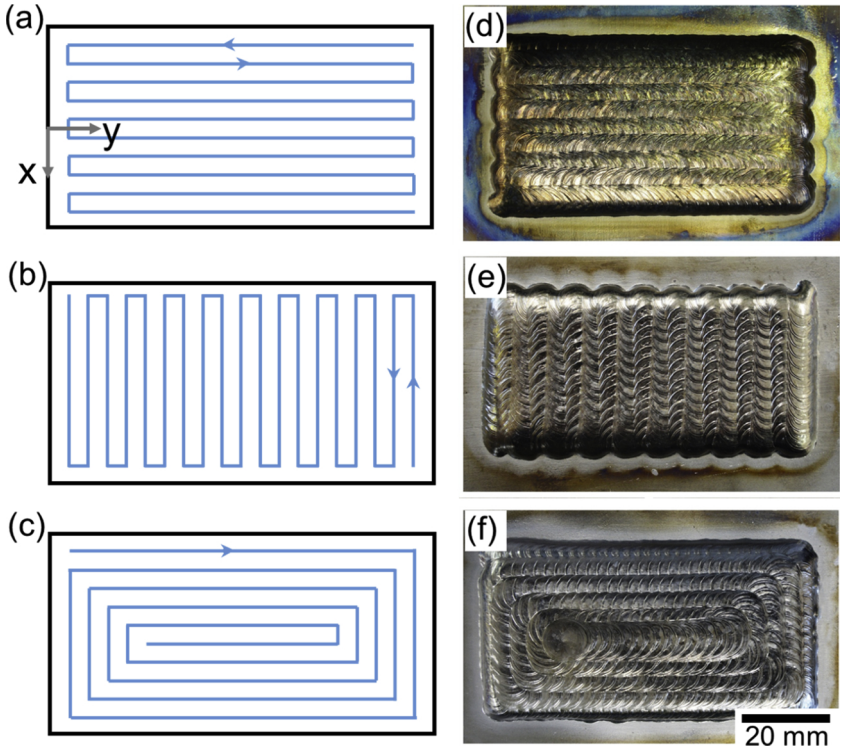

Fig. 2. Deposition patterns for the rectangular components with (a) long deposition pattern, (b) short deposition pattern and (c) spiral deposition pattern, and the corresponding morphology of the Ti-6Al-4V components deposited by (d) long deposition pattern, (e) short deposition pattern and (f) spiral deposition pattern.

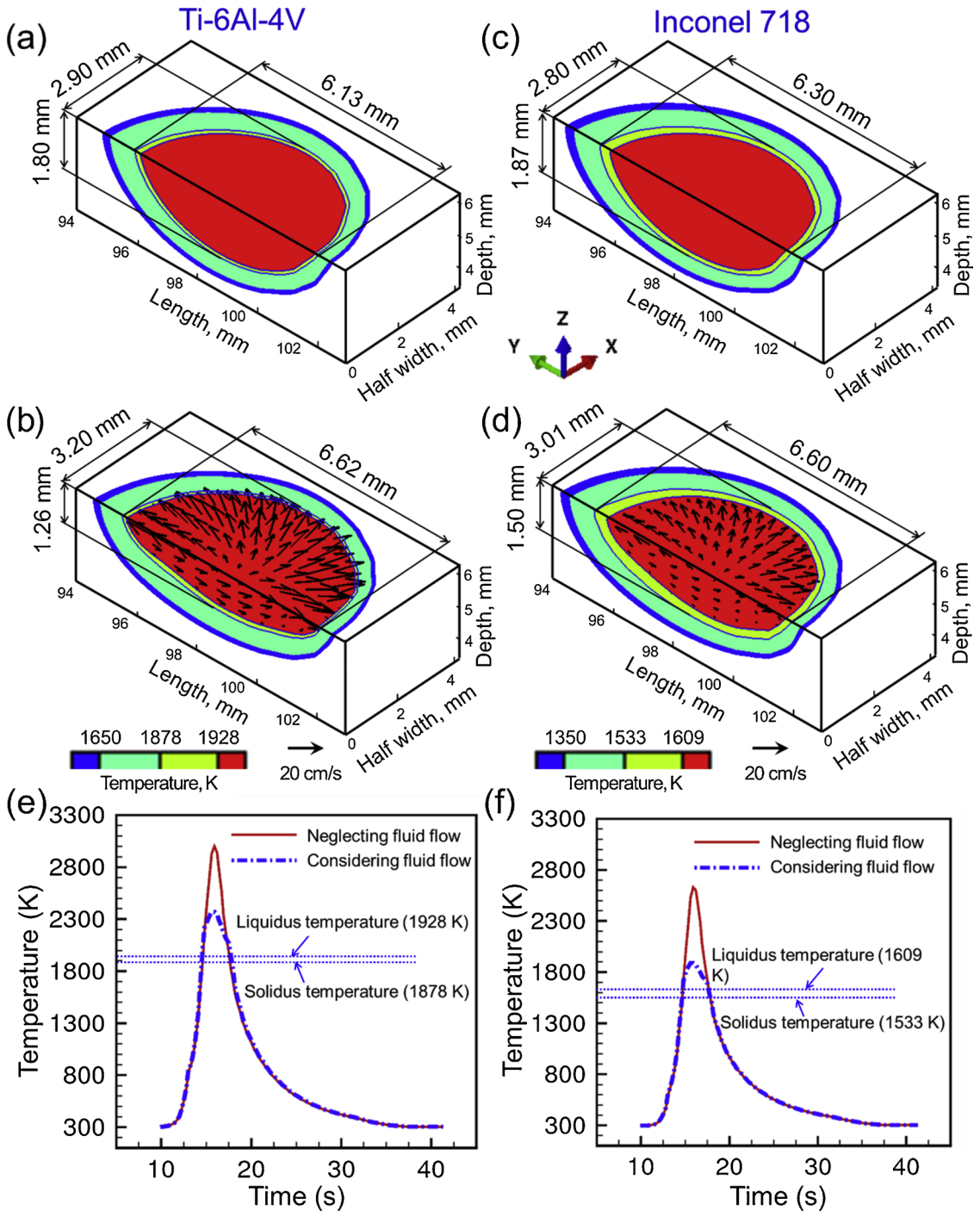

Fig. 3. Temperature distribution near the molten pool for Ti-6Al-4V calculated (a) neglecting fluid flow and (b) considering fluid flow. Temperature distribution near the molten pool for Inconel 718 calculated (c) neglecting fluid flow and (d) considering fluid flow. Molten pool dimensions are indicated in the figures. Half of the molten pools are shown because of the symmetry about yz plane. Scanning direction is along negative y-axis. Comparison of temperature variation with time for 72 mm long single-track deposits of (e) Ti-6Al-4V and (f) Inconel 718 calculated considering and neglecting fluid flow. The monitoring location is on the top surface at the mid length and mid width of the deposit. All processing parameters are the same as in Table 1.

consists of a computer numerical control (CNC) table with three degrees of freedom (x, y and z), a chamber filled with argon, a gas tungsten arc welding (GTAW) equipment and a wire feeder [13]. Since the deposits are rectangular in shape, rectangular substrates are used for convenience. The detailed dimensions of the deposit and substrate are shown in Fig. 1. The hot rolled substrate of same material as the feeding wire was mechanically polished before use. The substrate was restricted with four clamps at the four corners during the deposition process, as indicated in Fig. 1. The deposition parameters are listed in Table 1.

Three rectangular deposits of the same size were fabricated using three different deposition patterns, long, short and spiral patterns. The schematic for the three deposition patterns are shown in Fig. 2 (a–c). For long deposition pattern, the scanning direction was along the longer side of the rectangular deposit as shown in Fig. 2(a). However, the scanning direction was reversed between two successive hatches. For short deposition pattern, the scanning direction was along the shorter side of the rectangular deposit as shown in Fig. 2(b). Similar to long deposition pattern, the scanning direction was also reversed between

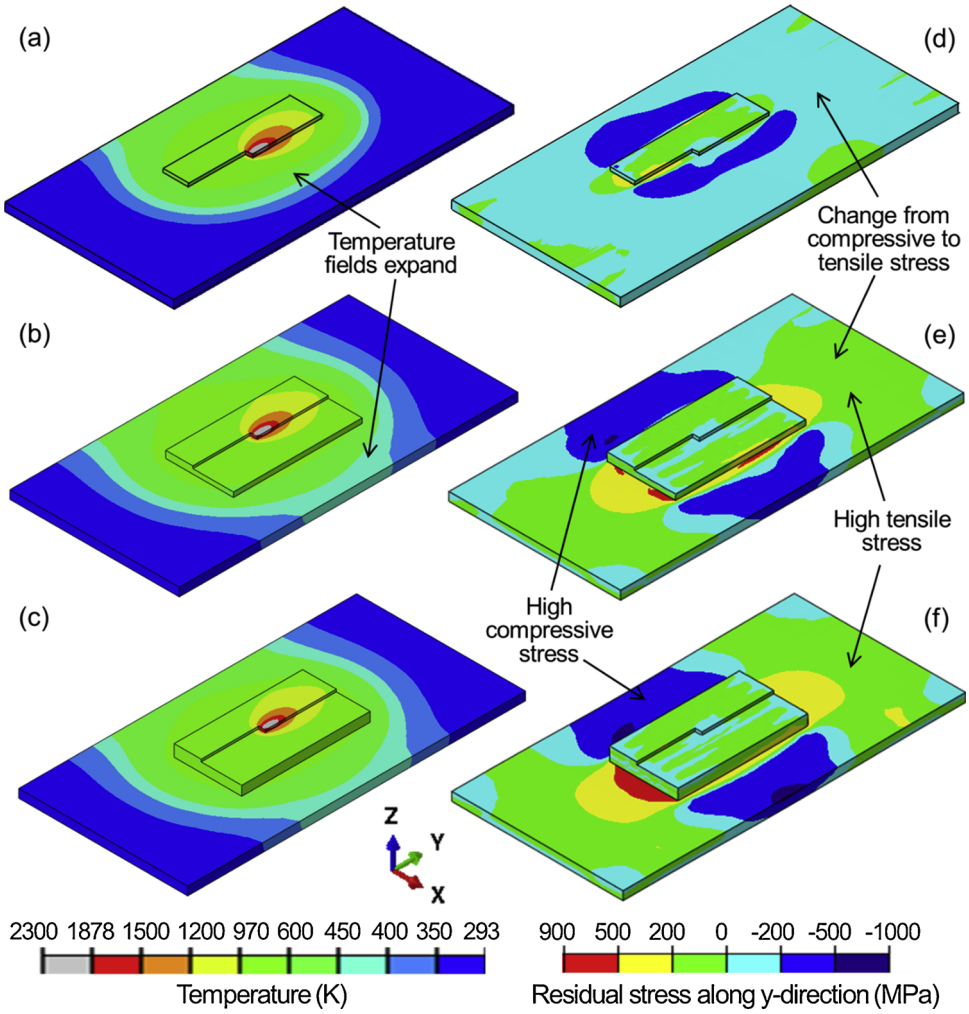

Fig. 4. The temperature distribution of Ti-6Al-4V part at the middle of the deposition of the (a) first layer, (b) third layer, (c) fifth layer and the corresponding y-component of stress distribution (longitudinal stress) of Ti-6Al-4V part during the deposition of (d) first layer, (e) third layer and (f) fifth layer. The results are for long deposition pattern using the processing conditions provided in Table 1.

two successive hatches. In the spiral deposition pattern, the arc followed a spiral path to deposit the rectangular component as shown in Fig. 2(c). All three deposits were made of five layers. For all three deposition patterns, the deposition of a particular layer started from the location where the deposition of the previous layer finished. Therefore, there was no idle time between layers. A cooling time of 800 s was provided at the end of the deposition after which the clamps were released. A constant hatch spacing of 4 mm was used for all deposition patterns.

The deposits fabricated with the three deposition patterns are shown in Fig. 2(d–f). The figures show that these deposits were successfully fabricated with no discontinuity, humps or splash around the corners. The contour of the component fabricated using long deposition pattern has undulations along the shorter sides of the deposit (Fig. 2d). In contrast, undulations are found along the longer sides in the component printed using short raster pattern (Fig. 2e). The component deposited using spiral pattern (Fig. 2f) has a relatively smoother contour than the other two patterns.

The residual stresses were measured using hole drilling method [14] at two locations (P1 and P2 in Fig. 1) on the top surface of the deposits at the end of the deposition process after the removal of clamps. Two holes with a diameter and depth of 1.5 mm and 2 mm respectively were drilled at the two specified locations. Three-element gauges were positioned around the hole to measure the strains based on which residual stresses were calculated. Although the experiments provided local values of strains and residual stresses, these measurements do not provide the 3D distribution of residual stresses in the components. Therefore, numerical calculations are performed to estimate residual stresses and distortion as discussed below.

3. Calculation of residual stresses and distortion in 3D

Calculation of residual stresses and distortion requires an accurate estimation of the 3D transient temperature field. Therefore it is important to examine the accuracy of the temperature field. The convective flow of molten metal often dominates the heat transfer mechanism inside the molten pool. We used a well-tested heat transfer and fluid flow model [2,4,15] to calculate the temperature field both considering and neglecting the convective flow of molten metal for the processing conditions used in the experiments. Fig. 3 (a) and (b) show the temperature fields near the molten pool for Ti-6Al-4V calculated neglecting and considering the convective flow of molten metal respectively. The convective flow inside the pool is radially outward and results in wider and shallower pool [16]. Therefore, the molten pool length and width in Fig. 3 (b) are higher than those in Fig. 3 (a). However, pool in Fig. 3 (b) is shallower than that in Fig. 3 (a). Similar observations can be made for Inconel 718 as evident from Fig. 3 (c) and (d). Ti-6Al-4V has lower density than IN 718 which is supposed to result in a larger molten pool for Ti-6Al-4V. However, IN 718 has much lower liquidus and solidus temperatures than those for Ti-6Al-4V. Due to the

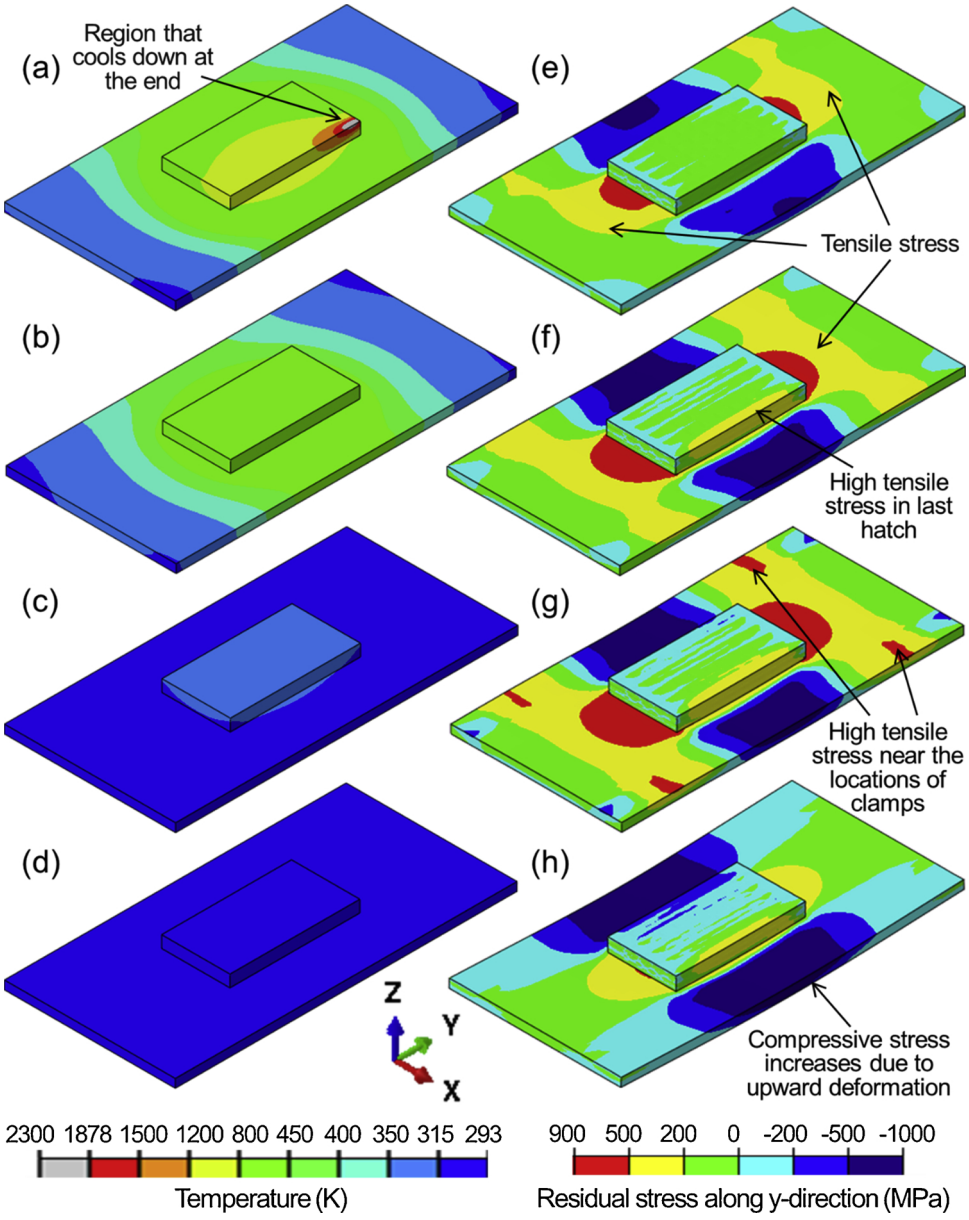

Fig. 5. The temperature distribution of Ti-6Al-4V part (a) at the beginning of cooling, (b) at the cooling time of 100 s, (c) at the cooling time of 500 s and (d) when the components have cooled down to room temperature and the clamps are released and the corresponding y-component of stress distribution (longitudinal stress) of Ti-6Al-4V part (e) at the beginning of cooling, (f) at the cooling time of 100 s, (g) at the cooling time of 500 s and (h) when the components have cooled down to room temperature and the clamps are released. The results are for long deposition pattern using the processing conditions provided in Table 1.

opposite effects of density and solidus and liquidus temperatures, molten pool sizes for the two alloys are almost identical. Fig. 3 (e) and (f) show that the calculations neglecting the fluid flow overestimates the temperature inside the molten pool for Ti-6Al-4V and IN 718 respectively. However, the fluid flow inside the molten pool does not have significant effect on the temperature variation below the solidus temperature. Therefore, the temperature values during cooling calculated considering fluid flow are same as that estimating by neglecting fluid flow as shown in Fig. 3 (e) and (f). Since residual stresses primarily depend on the temperature fields during the cooling time [2], convective flow does not have significant effect on residual stresses for the processing conditions studied and thus neglected in this research to make calculations tractable.

In this research, we used a thermo-mechanical model that calculates 3D, transient temperature field without considering the effect of convective flow based on which residual stresses and distortion were estimated. The processing conditions are provided in Table 1, which are the same as used for experiments. The following simplified assumptions were made in the thermo-mechanical model to make the calculations tractable.

(1) The surfaces of the deposited layers were considered to be flat.
(2) The densities of the solid and liquid metals were assumed to be independent of temperature.
(3) An approximate double ellipsoid heat source [17] was considered, whose dimensions were assumed to be constant during the whole deposition process. This assumption was made mainly because in a multi-layer, multi-hatch deposit, molten pool tends to attain a steady state after depositing a few tracks [18,19]. The dimensions of the heat source were approximately estimated from a single track deposit.
(4) Effect of solid state phase transformation [20] was neglected in the calculation of stresses.

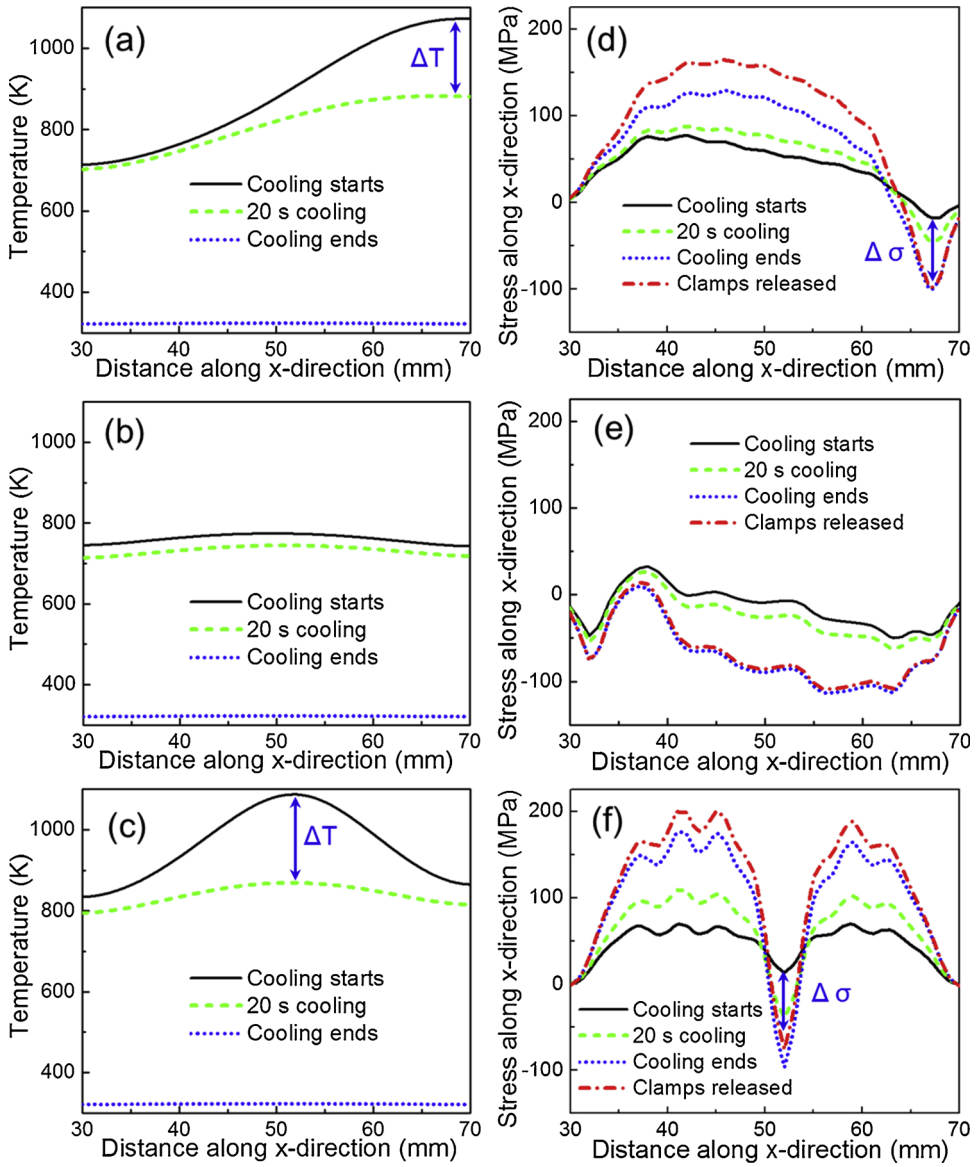

Fig. 6. Variation in temperature distribution along line 1 (shown in Fig. 1) during cooling for the Ti-6Al-4V deposit fabricated using (a) long deposition pattern, (b) short deposition pattern and (c) spiral deposition pattern. Similarly, the corresponding stresses along x-direction for the Ti-6Al-4V deposit made using (d) long deposition pattern, (e) short deposition pattern and (f) spiral deposition pattern during cooling. The results are for the three deposition patterns using the processing conditions provided in Table 1. ΔT and $\Delta\sigma$ represent the largest variations in temperature and residual stresses, respectively.

3D transient temperature field was calculated by solving the heat conduction equation [21] where the heat input was applied using an approximate double ellipsoidal heat source [17]. Finite element software Abaqus was used for the calculations [22]. The effect of liquid to solid transformation was considered by including the latent heat of fusion in the total enthalpy. Boundary conditions in these calculations included the heat losses by both radiation and convection from the surfaces of the deposit and substrate [6]. The convection coefficient [6] was taken as 5.7 W/(m^{2}K). However, a high value of 100 W/(m^{2}K) was used for the bottom surface of the substrate to consider the large amount of heat transfer through the cold workbench. Temperature-dependent thermo-physical and mechanical properties of Ti-6Al-4V and IN 718 used in the calculations were either taken from the literature [6,23–25] or calculated using a commercial software, JMatPro [4] and are provided in the Supplementary document. Temperature dependent material properties were applied using an "element birth technique" where small blocks of elements were activated based on the movement of the heat source simulated using a self-developed user subroutine. The calculated temperature distributions were then used to estimate the residual stresses and distortion.

The total strain that causes the distortion of the component includes elastic strain ($\Delta\varepsilon^E$), plastic strain ($\Delta\varepsilon^P$), thermal strain ($\Delta\varepsilon^{Th}$) and the strain caused by phase transformation and creep ($\Delta\varepsilon^{Tr}$) as follows [2].

$$\Delta\varepsilon^{tot} = \Delta\varepsilon^E + \Delta\varepsilon^P + \Delta\varepsilon^{Th} + \Delta\varepsilon^{Tr} \quad (1)$$

The elastic stress was calculated from the elastic strain by Hooke's law with temperature-dependent Young's modulus and Poisson's ratio [26]. The flow stress and plastic strain with temperature-dependent plasticity were calculated using the von Mises yield criterion [27]. The thermal strain was computed with the temperature-dependent coefficient of thermal expansion [26]. $\Delta\varepsilon^{Tr}$ was neglected in this model for simplicity. Calculations of residual stresses and distortion were also performed using the finite element based software Abaqus [22]. The substrate was restricted with four clamps at the four corners of the substrate as shown in Fig. 1. Therefore, the boundary conditions for the mechanical model was applied by constraining the movements of the

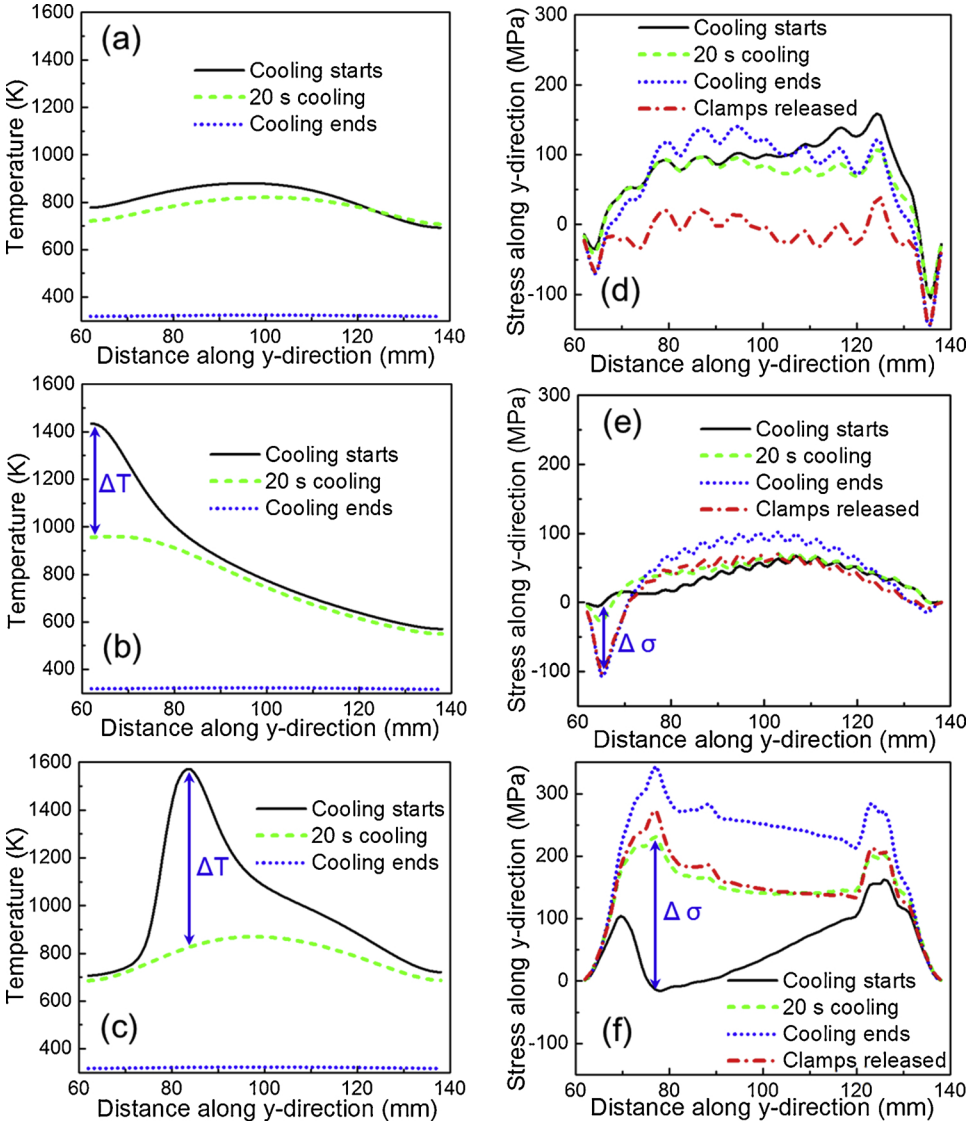

Fig. 7. Variation in temperature distribution along line 2 (indicated in Fig. 1) for the Ti-6Al-4V deposit made using (a) long deposition pattern, (b) short deposition pattern and (c) spiral deposition pattern during cooling. Similarly, the corresponding stresses along y-direction for the Ti-6Al-4V deposit fabricated using (d) long deposition pattern, (e) short deposition pattern and (f) spiral deposition pattern during cooling. The results are for the three deposition patterns using the processing conditions provided in Table 1. ΔT and $\Delta \sigma$ represent the largest variations in temperature and residual stresses, respectively.

nodes under the four clamps. When the printing was done and the substrate cooled down to the room temperature, clamp removal was simulated by deactivating the constraints from these nodes.

4. Results and discussions

To investigate the effects of transient temperature fields on the evolution of stresses during the deposition and cooling process, the Ti-6Al-4V component fabricated using long deposition pattern is selected as an example. Temperature fields and the corresponding stress distributions at the middle of the deposition of the first, third and fifth layers are shown in Fig. 4 (a–f). During the deposition of the first layer, both the substrate and the deposit are heated up intensively and the largest expansion in the deposit takes place along the scanning direction (along y-axis). Since the substrate is constrained by the clamps, it suffers from compressive stress, as shown in Fig. 4 (d). For upper layers, more heat accumulates that increases the temperature. The temperature fields during the deposition of the third layer (Fig. 4 b) are more expanded than that during the first layer (Fig. 4 a). Temperature fields nearly attain a steady state after the third layer. Therefore, when the arc moves from the center of the third layer to the center of the fifth layer, the temperature distribution in the substrate does not change significantly as shown in Fig. 4 (c). When the third layer is deposited, the previous two layers have already cooled down and contracted largely along y-direction. The contraction is dominant along y-direction because scanning is performed along y-axis in the long deposition pattern. Since the clamps restrict the deformation of the substrate, the contraction in the deposit results in high tensile stress in the substrate along the y-direction as shown in Fig. 4 (e). Contraction of the deposit along y-direction also results in large compressive stress in the substrate near the longer side of the component as shown in Fig. 4 (e). Since the temperature fields reach steady state after the third layer, the stress distribution (tensile or compressive) remains the same but the magnitudes of the stresses continue to increase as shown in Fig. 4 (e) and (f). The stress that originate during the deposition as shown in Fig. 4 significantly contribute to the final residual stresses fields. In other words, the evolution of stresses fields during cooling starts from the stress distributions that have already originated during deposition as explained below.

During the cooling process, the temperatures of the substrate and

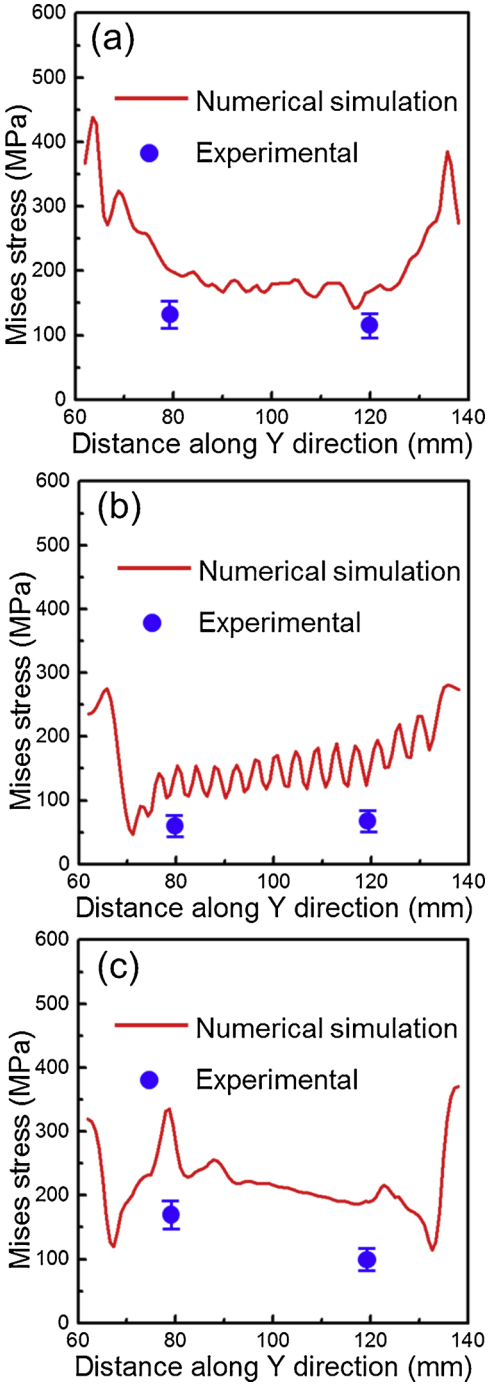

Fig. 8. Comparison of experimentally measured and numerically computed Mises stresses for Ti-6Al-4V components fabricated using (a) long deposition pattern, (b) short deposition pattern and (c) spiral deposition pattern. These results are taken along line 2 at two pinots P1 and P2 in Fig. 1. The processing conditions are provided in Table 1.

deposit continue to decrease as shown in Fig. 5 (a–c). At the end of the cooling, the deposit cools down to the room temperature and the clamps are released as shown in Fig. 5 (d). The deposit continues to shrink along y-direction during the whole cooling process. This contraction generates high tensile stresses in the substrate because the substrate is constrained by the clamps. This contraction also results in high compressive stress in the substrate near the longer edge of the component as shown in Fig. 5 (e). Magnitudes of these stresses continuously increase during the cooling process as shown in Fig. 5 (e–g). The last hatch of the 5th layer cools down at the end. Therefore, high tensile stresses are accumulated in this region as shown in Fig. 5 (f–g). This can be attributed to the fact that there is no subsequent heating operation on the last hatch to partially alleviate the stresses. In contrast, the stress values in the previously deposited hatches are partially alleviated due to reheating during the deposition of subsequent hatches. Similar observation was also made by Mughal et al. [8] during multi-layer WAAM of a mild steel component. Since the clamps constraint the substrate to contract, the substrate largely suffers from tensile stress, especially in the region close to the clamps and the region near the edge of the shorter side of the deposit, as shown in Fig. 5 (g). After releasing the clamps, the shorter edges of the substrate deform upward and thus the high tensile stresses near the clamps are relieved as shown in Fig. 5 (h). Upward deformation results in high compressive stress on the top surface of the substrate near the longer side of the deposit as shown in Fig. 5 (h). From Figs. 4 and 5 it is evident that the residual stresses and distortion evolve depending on the transient temperature field and are largely controlled by the deposition pattern. Therefore, the stresses of Ti-6Al-4V components printed using three different deposition patterns are compared below.

To compare the x-component of residual stresses for three deposition patterns, variations in temperature and resulting stress evolutions have been investigated during the cooling process. Fig. 6 (a–f) show the variations in temperature and x-component of stresses along line 1 (Fig. 1) at different time during cooling of Ti-6Al-4V components fabricated using three deposition patterns. For the deposit fabricated using short deposition pattern, change in temperature along line 1 (Fig. 6 b) during cooling is very less which results in low residual stresses in the component (Fig. 6 e). However, for the component made using long deposition pattern, largest change in temperature (ΔT) is observed near the long edge of the deposit where the last hatch is deposited as shown in Fig. 6 (a). This large variation in temperature during cooling results in sharp change [28] in residual stresses ($\Delta\ \sigma$) at the same location as shown in Fig. 6 (d). For the spiral deposition pattern, the region near the center of the deposit cools down to the room temperature at the end. Therefore, the largest change in temperature (ΔT) is observed at the mid-length of line 1 as shown in Fig. 6 (c). This large variation in temperature results in sharp change in residual stresses ($\Delta\ \sigma$) at the same location as shown in Fig. 6 (f).

Fig. 7 shows the variations in temperature and y-component of stresses along line 2 (Fig. 1) at different time during cooling for the components fabricated using three deposition patterns. For the deposit fabricated using the long deposition pattern, change in temperature along line 2 (Fig. 7 a) during cooling is very less. Therefore, there is no significant change in the stress field during the cooling as shown in Fig. 7 (d). However, sudden change of stresses from tensile to compressive occurs due to the removal of the clamps as explained before. For the component made using short deposition pattern, largest change in temperature (ΔT) is observed near the short edge of the deposit where the last hatch is deposited as shown in Fig. 7 (b). This large variation in temperature during cooling results in sharp change in residual stresses ($\Delta\ \sigma$) at the same location as shown in Fig. 7 (e). For the spiral deposition pattern, the region near the center of the deposit cools down to the room temperature at the end. Therefore, the largest change in temperature is observed near the mid-length of line 2 as shown in Fig. 7 (c). This large variation in temperature results in sharp change in residual stresses at the same location as shown in Fig. 7 (f).

The aforementioned calculated stress results show fair agreement with the experimental measurements. For example, Fig. 8 shows that the calculated Mises residual stresses along line 2 (Fig. 1) agree with the corresponding experimental results for Ti-6Al-4V deposits printed using the three deposition patterns. The slight mismatch between the computed and experimental results is primarily caused by the measurement error of hole drilling method and the assumptions made in the thermo-mechanical model. It is evident from the figure that along the same line the residual stresses can be significantly different depending on the deposition pattern used. These differences can be more pronounced for

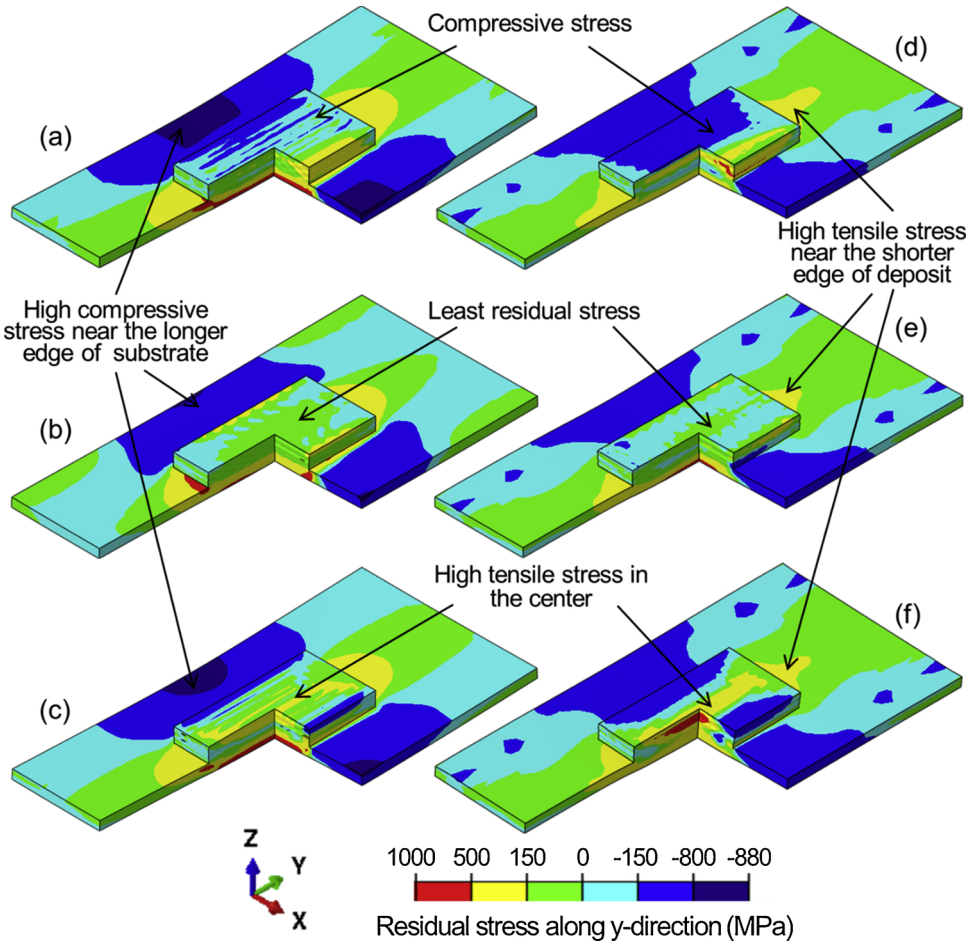

Fig. 9. Residual stresses along y-direction in the Ti-6Al-4V components fabricated using (a) long deposition pattern, (b) short deposition pattern and (c) spiral deposition pattern when the deposits cooled down to room temperature and the clamps were released. Residual stresses along y-direction in the Inconel 718 components deposited with (d) long deposition pattern, (e) short deposition pattern and (f) spiral deposition pattern when the deposits cooled down to room temperature and the clamps were released. The processing conditions are provided in Table 1.

various alloy systems with different thermo-physical and mechanical properties. To investigate the simultaneous effects of deposition patterns and alloys, the stresses and deformation of the components made using three different deposition patterns are calculated for Ti-6Al-4V and IN 718 as explained below.

Fig. 9 shows the y-component of the residual stresses in both alloys fabricated with three deposition patterns after releasing the clamps. Cutaway isometric views are used to show the accumulations of residual stresses inside the component. For both alloys, the y-direction stress distributions in the substrate are the same with high tensile stress near the shorter edge of the deposit and high compressive stress near the longer edge of the substrate. Y-direction stresses mainly originate from the expansion along this direction during heating and shrinkage during cooling. During the cooling time, all deposits shrink resulting in high tensile stresses near the shorter edge of the deposit. For the region near the longer edge of the substrate, compressive stresses originate due to the upward bending of shorter edges of the substrate after releasing the clamps. For the components fabricated with long deposition pattern (Fig. 9 a and d), compressive stresses are observed on the top surface of the deposits because y-direction is the primary contraction direction for the deposit with long deposition pattern. For both alloys, high tensile stresses can be found in the center of the deposit with spiral deposition pattern (as shown in Fig. 9 c and f) since the last hatch is deposited at that location. For both alloys, the deposits made using short deposition pattern (Fig. 9 b and e) have the least residual stresses among the three deposition patterns. This is because more hatches needed to fabricate the deposits using short deposition pattern significantly alleviate the stresses due to the reheating effect. It can also be found that after clamp removal, high tensile stresses accumulate on the bottom of the substrates for both alloys due to the upward bending of the substrates.

The x-component of the residual stresses for both alloys fabricated using three deposition patterns are shown in Fig. 10. For both alloys and all three deposition patterns, high x-direction tensile stresses originate perpendicular to the x-axis near the longer edge of the deposit due to the contraction during cooling. High compressive stresses can be found near the shorter edge of the deposit to balance the tensile stresses in the substrate. For both alloys, compressive stresses can be found on the surface of the deposit printed using short deposition pattern (Fig. 10 b and e) because x-direction is the primary contraction direction for that deposit. In addition, for both alloys, the deposits with spiral pattern (Fig. 10 c and f) have the highest stresses values compared to the other depositions.

Delamination of the component mainly depends on the stresses (σ) at the substrate-deposit interface and the yield stress (Y) of the alloy at room temperature. A delamination index, d^*, is proposed here to evaluate the susceptibility to delamination of WAAM components and is expressed as:

$$d^* = \sigma/Y \tag{2}$$

For both the alloys, two lines (line 3 and 4 as indicated in Fig. 1) are selected at the substrate-deposit interface to study the influence of different deposition patterns on delamination of the components. Stress

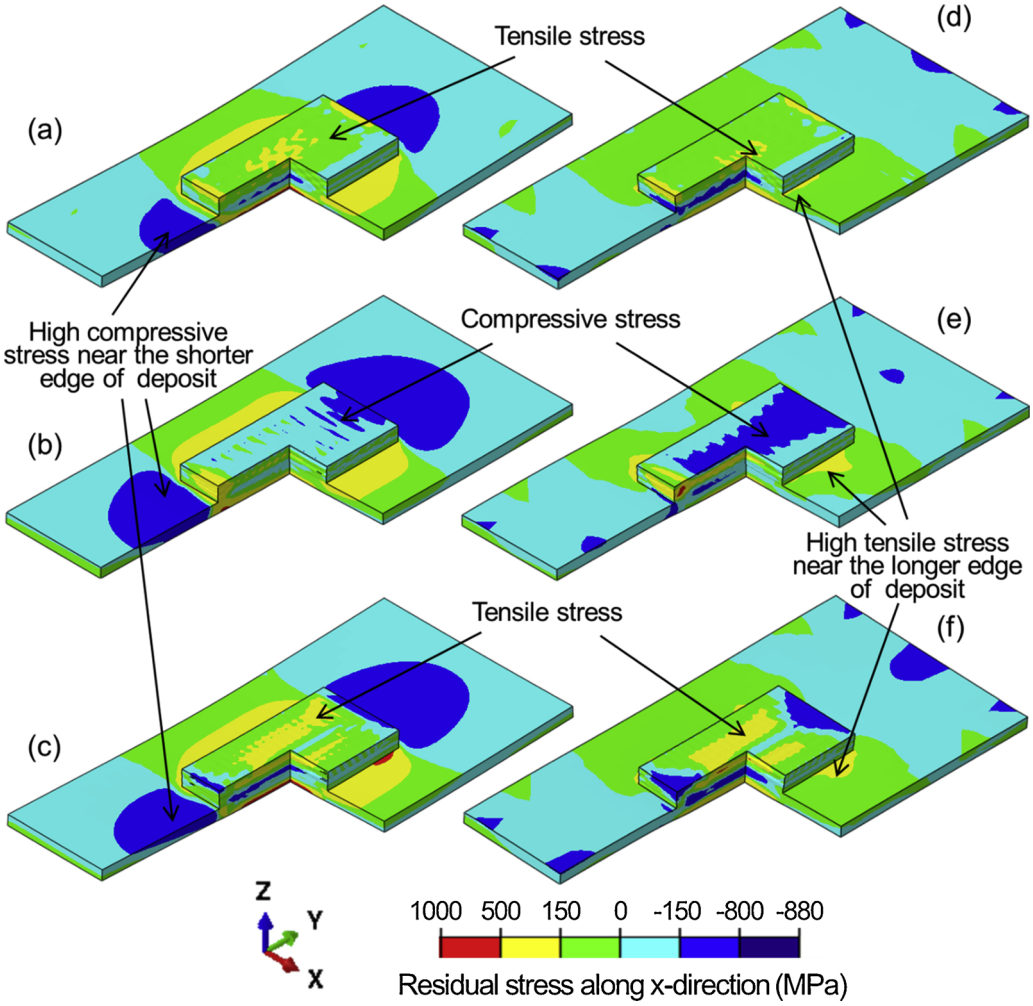

Fig. 10. Residual stresses along x-direction in the Ti-6Al-4V components fabricated using (a) long deposition pattern, (b) short deposition pattern and (c) spiral deposition pattern when the deposits cooled down to room temperature and the clamps were released. Residual stresses along x-direction in the Inconel 718 components deposited with (d) long deposition pattern, (e) short deposition pattern and (f) spiral deposition pattern when the deposits cooled down to room temperature and the clamps were released. The processing conditions are provided in Table 1.

components along x and y directions are considered to calculate the delamination index along line 3 and 4, respectively. Fig. 11 (a–f) show that for a particular pattern, the stress distributions for both alloys are similar. However, the magnitudes of stresses are different because of the dissimilar mechanical properties of the two alloys. Fig. 11 (g–l) shows the corresponding delamination index for both the alloys along line 3 and 4 respectively. The delamination index is much higher in IN 718 components than that in Ti-6Al-4V parts (Fig. 11 j–l). This is mainly because the delamination depends on both the stresses at the substrate-deposit interface and the yield stress of the alloy at room temperature. The stresses at the interface are often higher for Ti-6Al-4V components. However, the room-temperature yield strength of Ti-6Al-4V is around 3 times higher than that of IN 718. Therefore, Ti-6Al-4V is less susceptible to delamination than IN 718 for a given set of processing conditions.

Warping of the components primarily depends on the vertical deformation (u_z) of the component and the substrate thickness (d). A warping index, w^*, is proposed here to evaluate the susceptibility to warping for AM components and is expressed as:

$$w^* = u_z / d \tag{3}$$

Fig. 12 shows the warping index along line 4 (Fig. 1) for the components fabricated with three deposition patterns under the same processing conditions for both alloys. It can be found that in the substrate-deposit interface, the warping is similar for both alloys with a certain deposition pattern, which can be attributed to the similar molten pool size of the two alloys (Fig. 3). For both alloys, the warping of the deposits with long and spiral deposition patterns is higher than that with short deposition pattern. Since shorter tracks shrink less during cooling, the component fabricated with short deposition pattern exhibits the least deformation and warping among the three deposition patterns.

From the aforementioned results, it is evident that for a particular set of processing conditions and deposition pattern, components fabricated with different alloys exhibit remarkably diverse residual stresses and distortion. Rigorous numerical models similar to what used in this research are helpful to understand this effect. However, these models are computationally intensive and cannot be used in real time. Therefore, a recently proposed non-dimensional strain parameter, ε^*, is used as an indicator of susceptibility to deformation [29,30]:

$$\varepsilon^* = (\beta \Delta T/EI)^* t^* (H^{3/2}/F\sqrt{\rho}) \tag{4}$$

where β is the volumetric coefficient of thermal expansion, ΔT is the maximum rise in temperature during the process, E is the elastic modulus and I is the moment of inertia of the substrate, the product, EI, is the flexural rigidity of the substrate, t is the characteristic time that equals to the total time required to deposit a single layer, H is the heat input per unit length, F is the Fourier number [31] and ρ is the density of the alloy. The peak temperature and the depth of the molten pool can be calculated using the thermo-mechanical model. This strain

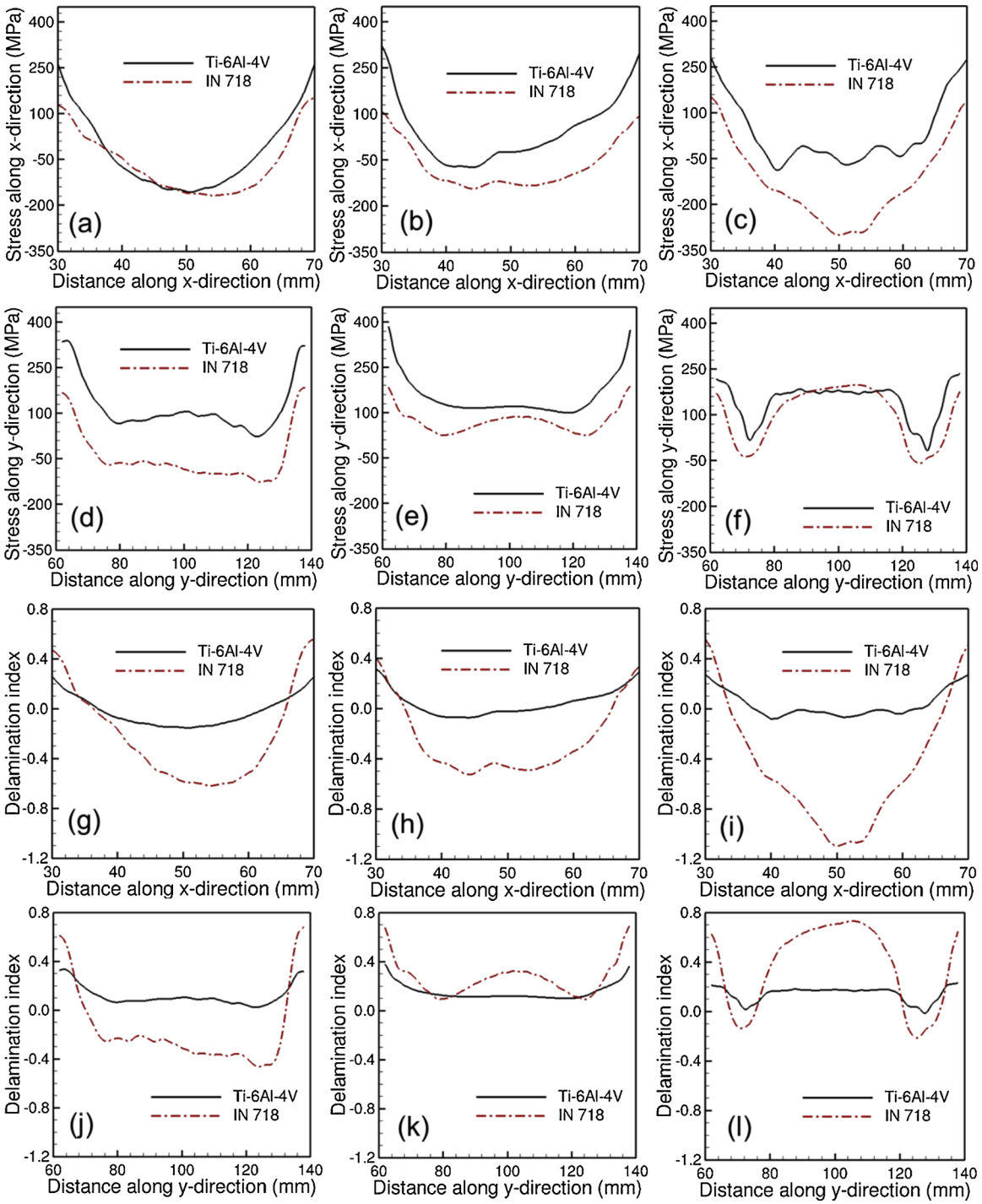

Fig. 11. Calculated x-component of residual stresses along line 3 (indicated in Fig. 1) in the parts fabricated using (a) long deposition pattern, (b) short deposition pattern and (c) spiral deposition pattern after releasing the clamps. Calculated y-component of residual stresses along line 4 in the components fabricated using (d) long deposition pattern, (e) short deposition pattern and (f) spiral deposition pattern after releasing the clamps. Correspondingly, the delamination index along line 3 in the components deposited with (g) long deposition pattern, (h) short deposition pattern and (i) spiral deposition pattern after releasing the clamps. The delamination index along line 4 in the components deposited with (j) long deposition pattern, (k) short deposition pattern and (l) spiral deposition pattern after releasing the clamps. The processing conditions are provided in Table 1. Delamination index is the ratio of the residual stresses at the substrate-deposit interface to the yield strength of the alloy at room temperature.

parameter quantitatively represents the maximum strain encountered by the fabricated component [31]. From Eq. (4), it's obvious that strains increase with rise in temperature and heat input, but decrease with increasing flexural rigidity of the substrate. The maximum strain during the deposition is calculated using the thermo-mechanical model at three different heat inputs for both the alloys. The strain parameter is also calculated for the corresponding processing conditions for two alloys. Fig. 13 shows that the numerically calculated maximum strains in the single-track deposit are consistent with the strain parameter, ε^*, for both the alloys at different heat input. With the increase in heat input, the strain increases because larger molten pools shrink more during solidification and exhibit more distortion. It can also be found that for a particular heat input, the strain parameters for both the alloys are similar, which is attributed to the similar size of molten pool of

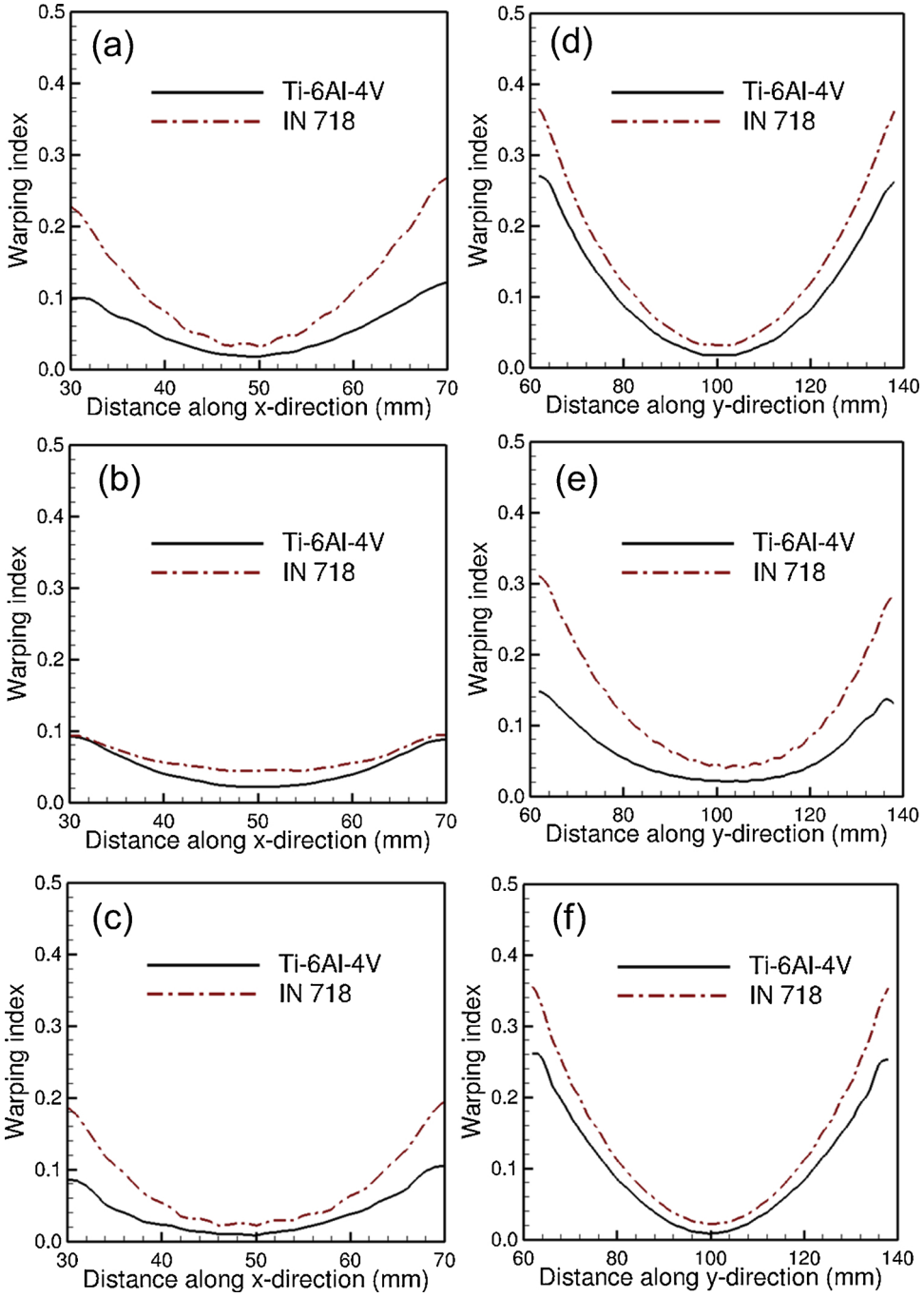

Fig. 12. Warping index along line 3 (shown in Fig. 1) in the components fabricated with the same substrate thickness using (a) long deposition pattern, (b) short deposition pattern and (c) spiral deposition pattern after releasing the clamps. Warping index along line 4 in the components fabricated with the same substrate thickness using (d) long deposition pattern, (e) short deposition pattern and (f) spiral deposition pattern after releasing the clamps. The processing conditions are provided in Table 1. Warping index is the ratio of vertical deformation of the component to the substrate thickness.

these two alloys (Fig. 3). Therefore, back-of-the-envelope calculations using the strain parameter can be helpful for shop floor usage.

5. Summary and conclusions

We used a combined theoretical and experimental investigation to reveal the influence of three deposition patterns on residual stresses and distortion of multi-layer WAAM components of Ti-6Al-4V and Inconel 718. Below are the specific findings.

1) For both alloys, convective flow of molten metal was found to affect the peak temperature, the temperature distribution inside the pool as well as fusion zone shape and size. However, for the conditions of the experiments reported here, the temperature field during cooling below the solidus temperature were not significantly affected by convection. Since residual stresses primarily depend on the temperature variation during cooling of the solids, the convective flow was neglected in the thermo-mechanical model to make the calculations tractable.
2) Residual stresses can be mitigated by using short track lengths. Deposition patterns significantly influenced residual stresses and deformation of deposits with maximum residual stresses

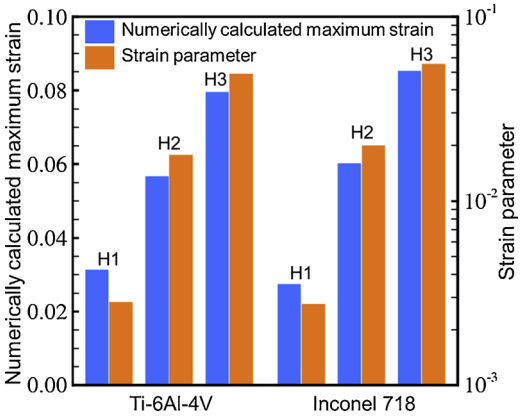

Fig. 13. Strain parameters and numerically calculated maximum strain for single-track deposits fabricated using three different heat inputs (H1 = 195 J/mm, H2 = 293 J/mm, and H3 = 390 J/mm,) for both alloys. Other processing conditions are the same as in Table 1. The same substrate dimensions (200 mm long, 100 mm wide, 5 mm thick) are taken for all the cases for consistency.

accumulated in deposits made by spiral tracks among the three deposition patterns investigated.

3) The magnitudes of stresses were different for the two alloys for the same processing conditions due to the differences in their mechanical properties. However, the 3D spatial distribution of residual stresses for the three different deposition patterns were similar for the two alloys. The components built with Ti-6Al-4V were not as vulnerable as Inconel 718 to delamination.
4) For both alloys, the center of the build fabricated with spiral deposition pattern cooled down at the end and accumulated very high residual stresses and distortion. In the deposits made using long and short deposition patterns, the locations that cool down at the end and accumulated high residual stresses were near the edge of the deposit.
5) Back-of-the-envelope calculations using a dimensionless strain parameter was found to capture the effects of process parameters on strain and deformation for both alloys investigated. The analytical calculations agreed with the results obtained from a rigorous thermo-mechanical model for both the alloys investigated. The relatively simple and easy-to-use strain parameter can be helpful for shop floor usage where rapid calculations are required, and computationally intensive large rigorous numerical models cannot be used.

Declaration of Competing Interest

None.

Acknowledgments

The work was supported by China Scholarship Council [grant number 201806030114]; and the National Natural Science Foundation of China [grant number 51875041].

Appendix A. Supplementary data

Supplementary material related to this article can be found, in the online version, at doi:https://doi.org/10.1016/j.addma.2019.100808.

References

[1] T. Debroy, H.L. Wei, J.S. Zuback, T. Mukherjee, J.W. Elmer, J.O. Milewski, et al., Additive manufacturing of metallic components – process, structure and properties, Prog. Mater. Sci. (2017).
[2] T. Mukherjee, W. Zhang, T. Debroy, An improved prediction of residual stresses and distortion in additive manufacturing, Comput. Mater. Sci. 126 (2017) 360–372.
[3] T. DebRoy, T. Mukherjee, J.O. Milewski, J.W. Elmer, B. Ribic, J.J. Blecher, et al., Scientific, technological and economic issues in metal printing and their solutions, Nat. Mater. (2019), https://doi.org/10.1038/s41563-019-0408-2.
[4] T. Mukherjee, J.S. Zuback, W. Zhang, T. Debroy, Residual stresses and distortion in additively manufactured compositionally graded and dissimilar joints, Comput. Mater. Sci. 143 (2018) 325–337.
[5] M. Somashekara, M. Naveenkumar, A. Kumar, C. Viswanath, S. Simhambhatla, Investigations into effect of weld-deposition pattern on residual stress evolution for metallic additive manufacturing, Int. J. Adv. Manuf. Technol. 90 (2017) 2009–2025.
[6] J. Ding, Thermo-mechanical Analysis of Wire and Arc Additive Manufacturing Process, Cranfield University, 2012.
[7] H. Zhao, G. Zhang, Z. Yin, L. Wu, Three-dimensional finite element analysis of thermal stress in single-pass multi-layer weld-based rapid prototyping, J. Mater. Process. Technol. 212 (2012) 276–285.
[8] M. Mughal, H. Fawad, R. Mufti, M. Siddique, Deformation modelling in layered manufacturing of metallic parts using gas metal arc welding: effect of process parameters, Model. Simul. Mat. Sci. Eng. 13 (2005) 1187.
[9] M.P. Mughal, R.A. Mufti, H. Fawad, The mechanical effects of deposition patterns in welding-based layered manufacturing, Proc. Inst. Mech. Eng. Part B J. Eng. Manuf. 221 (2007) 1499–1509.
[10] K. Oyama, S. Diplas, M. M'hamdi, A.E. Gunnæs, A.S. Azar, Heat source management in wire-arc additive manufacturing process for Al-Mg and Al-Si alloys, Addit. Manuf. 26 (2019) 180–192.
[11] P.J. Withers, H. Bhadeshia, Residual stress. Part 2–Nature and origins, Mater. Sci. Technol. 17 (2001) 366–375.
[12] V. Manvatkar, A. De, T. Debroy, Heat transfer and material flow during laser assisted multi-layer additive manufacturing, J. Appl. Phys. 116 (2014) 133.
[13] Q. Wu, J. Lu, C. Liu, X. Shi, Q. Ma, S. Tang, et al., Obtaining uniform deposition with variable wire feeding direction during wire-feed additive manufacturing, Mater. Manuf. Process. (2017).
[14] P.J. Withers, H. Bhadeshia, Residual stress. Part 1–measurement techniques, Mater. Sci. Technol. 17 (2001) 355–365.
[15] T. Mukherjee, T. DebRoy, Printability of 316 stainless steel, Sci. Technol. Weld. Join. (2019) 1–8.
[16] W. Ou, T. Mukherjee, G.L. Knapp, Y. Wei, T. DebRoy, Fusion zone geometries, cooling rates and solidification parameters during wire arc additive manufacturing, Int. J. Heat Mass Transf. 127 (2018) 1084–1094.
[17] J. Goldak, A. Chakravarti, M. Bibby, A new finite element model for welding heat sources, Metall. Trans. B 15 (1984) 299–305.
[18] Y. Lei, J. Xiong, R. Li, Effect of inter layer idle time on thermal behavior for multi-layer single-pass thin-walled parts in GMAW-based additive manufacturing, Int. J. Adv. Manuf. Technol. 96 (2018) 1355–1365.
[19] J. Ding, P. Colegrove, J. Mehnen, S. Ganguly, P.S. Almeida, F. Wang, et al., Thermo-mechanical analysis of Wire and Arc Additive Layer Manufacturing process on large multi-layer parts, Comput. Mater. Sci. 50 (2011) 3315–3322.
[20] J. Ahn, E. He, L. Chen, R. Wimpory, J. Dear, C. Davies, Prediction and measurement of residual stresses and distortions in fibre laser welded Ti-6Al-4V considering phase transformation, Mater. Des. 115 (2017) 441–457.
[21] K. Khan, A. De, Modelling of selective laser melting process with adaptive re-meshing, Sci. Technol. Weld. Join. (2019) 1–10.
[22] Abaqus Documentation, Version 6.14, Dassault Systems, (2015).
[23] T. Seshacharyulu, S. Medeiros, J. Morgan, J. Malas, W. Frazier, Y. Prasad, Hot deformation and microstructural damage mechanisms in extra-low interstitial (ELI) grade Ti–6Al–4V, Mater. Sci. Eng. A 279 (2000) 289–299.
[24] P. Rangaswamy, High Temperature Stress Assessment in SCS-6/Ti-6A1-4V Composite Using Neutron Diffraction and Finite Element Modeling, Los Alamos National Lab., Los Alamos, NM (US), 2000.
[25] K.C. Mills, Recommended Values of Thermophysical Properties for Selected Commercial Alloys, Woodhead Publishing, 2002.
[26] A. Kamara, S. Marimuthu, L. Li, A numerical investigation into residual stress characteristics in laser deposited multiple layer waspaloy parts, J. Manuf. Sci. Eng. 133 (2011) 031013.
[27] D. Deng, H. Murakawa, Numerical simulation of temperature field and residual stress in multi-pass welds in stainless steel pipe and comparison with experimental measurements, Comput. Mater. Sci. 37 (2006) 269–277.
[28] M. Strantza, B. Vrancken, M.B. Prime, C. Truman, M. Rombouts, D.W. Brown, et al., Directional and oscillating residual stress on the mesoscale in additively manufactured Ti-6Al-4V, Acta Mater. (2019).
[29] T. Mukherjee, V. Manvatkar, A. De, T. Debroy, Dimensionless numbers in additive manufacturing, J. Appl. Phys. 121 (2017).
[30] T. Mukherjee, V. Manvatkar, A. De, T. Debroy, Mitigation of thermal distortion during additive manufacturing, Scr. Mater. 127 (2017) 79–83.
[31] T. Mukherjee, J.S. Zuback, A. De, T. Debroy, Printability of alloys for additive manufacturing, Sci. Rep. 6 (2016) 1–6.